Record of modern-style plate tectonics in the Palaeoproterozoic Trans-Hudson orogen

O. M. Weller[1,2]* and M. R. St-Onge[1]

The Trans-Hudson orogen of North America is a circa 1,800 million year old, middle Palaeoproterozoic continental collisional belt. The orogen may represent an ancient analogue to the Himalayan orogen, which began forming 50 million years ago and remains active today. Both mountain belts exhibit similar length scales of deformation and timescales of magmatism and metamorphism. A notable divergence in this correlation has been the absence of high-pressure, low-temperature metamorphic rocks in the Trans-Hudson compared with the Himalaya. It has been debated whether this absence reflects a secular tectonic change, with the requisite cool thermal gradients precluded by warmer ambient mantle temperatures during the Palaeoproterozoic, or a lack of preservation. Here we identify eclogite rocks within the Trans-Hudson orogen. These rocks, which typically form at high pressures and cool temperatures during subduction, fill the gap in the comparative geologic record between the Trans-Hudson and Himalayan orogens. Through the application of phase equilibria modelling and *in situ* U–Pb monazite dating we show that the pressure–temperature conditions and relative timing of eclogite-facies metamorphism are comparable in both orogenies. The results imply that modern-day plate tectonic processes featuring deep continental subduction occurred at least 1,830 million years ago. This study highlights that the global metamorphic rock record (particularly in older terrains) is skewed by overprinting and erosion.

Tectonic regimes on Earth have undergone a secular change in style, with an early non-plate tectonic regime giving way to more uniformitarian plate tectonic processes featuring subduction, largely owing to planetary cooling and the resultant effects on lithospheric thickness and strength[1]. However, the timing at which this transition occurred is contested, with some authors considering near-uniformitarian tectonics as far back as the Mesoarchaean[2] (3,200–2,800 million years ago (Ma)), whereas others argue for a Neoarchaean[3] (2,800–2,500 Ma) or a Neoproterozoic[4] (1,000–541 Ma) onset of subduction. A secondary debate is how subduction-related processes have changed over time, with proponents of early subduction initiation suggesting that subduction zones have evolved from warmer Proterozoic regimes to cooler Phanerozoic regimes, with the latter marked by the emergence of high to ultrahigh pressure (UHP) metamorphism in the global rock record[5].

The Trans-Hudson orogen (THO) provides a unique opportunity to consider and resolve some of these issues as it comprises a superbly exposed middle Palaeoproterozoic continental collision belt that extends ∼3,000 km across North America (Fig. 1)[6,7]. Numerous studies of the THO have shown that it formed following closure of the Manikewan Ocean and terminal collision of the lower Superior and upper Churchill plates at about 1.83 billion years ago (Ga) (refs 8,9). Furthermore, several parallels have been drawn between the THO and the archetypical Himalayan orogen of central Asia—which formed following convergence between the lower Indian and upper Asian plates since about 50 Ma (ref. 10)—as both orogens are of a similar scale (Fig. 1) and exhibit similar patterns of magmatism and metamorphism with respect to the timing of collision (Supplementary Fig. 1)[11–15].

While the THO–Himalaya comparison would appear to undermine suggestions of a Neoproterozoic onset of subduction[4], a notable deviation in the correlation has been the absence of high-pressure rocks in the THO compared with a number of eclogite localities documented in the Himalaya[16–18]. On a more global scale, compilations of metamorphic thermal gradients through time[3,5,19,20] have shown that pre-Phanerozoic orogens are apparently largely characterized by an absence of thermal gradients of $<350\,°C\,GPa^{-1}$ (a threshold that delimits high-pressure–low-temperature metamorphic settings[5]), such that plate tectonic regimes are viewed as having undergone a fundamental transition during the late Neoproterozoic due to declining mantle temperatures, enabling subduction of continental material to mantle depths[20]. Alternatively, the signal may reflect a preservation bias, with older high-pressure assemblages more likely to have been overprinted by subsequent tectonothermal events, or lost to erosion.

Here we document a new discovery of eclogite from the THO. Through integrated phase equilibria modelling and *in situ* monazite dating we show that the THO eclogite is commensurate with eclogite at the type Himalayan Tso Morari locality, with both featuring similar field settings, pressure–temperature (*P–T*) cycles, and timings of metamorphism contemporaneous with the onset of continental collision. The results cement the THO–Himalayan comparison, show that cool thermal gradients ($<350\,°C\,GPa^{-1}$) were present in continental subduction zone settings in the Palaeoproterozoic, and ultimately unite the Phanerozoic and Proterozoic plate tectonic regimes.

Trans-Hudson eclogite field setting

Northern Quebec marks the north-eastern corner of the THO (Fig. 1), where two major lithotectonic packages are exposed: a lower plate domain comprising Archaean basement granulite-facies felsic orthogneiss (Superior craton) and overlying Palaeoproterozoic rift-fill sedimentary and volcanic strata (Povungnituk and Chukotat groups); and an upper plate domain (Churchill plate) comprising a Palaeoproterozoic obducted ophiolite (Watts Group)

[1]Geological Survey of Canada, 601 Booth Street, Ottawa, Ontario K1A 0E8, Canada. [2]Department of Earth Sciences, University of Cambridge, Downing Street, Cambridge CB2 3EQ, UK. *e-mail: ow212@cam.ac.uk
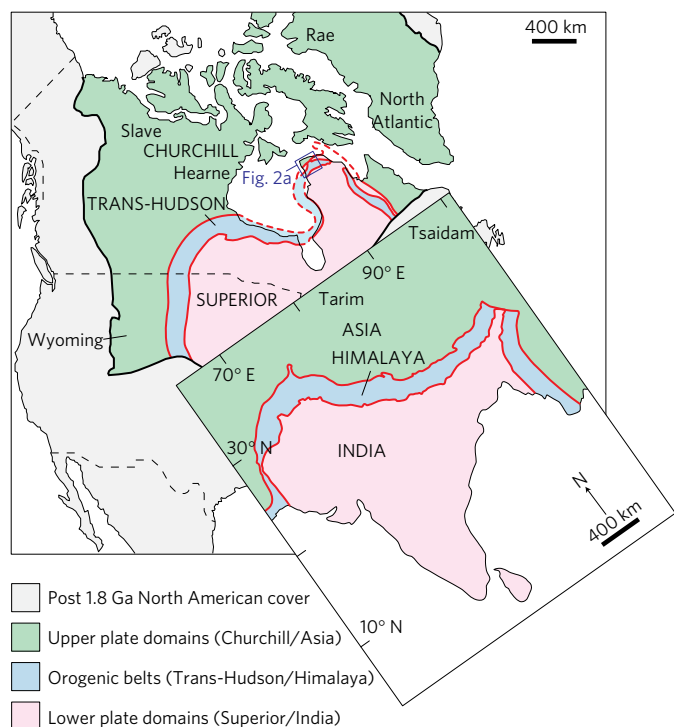
Figure 1 | Tectonic maps of the Palaeoproterozoic Trans-Hudson orogen and the Cenozoic Himalayan orogen showing their similar scale and orogenic architecture[11]. The upper plate of each orogen is shaded in green, the lower plate in pink and the metamorphic core in blue. Major lithotectonic domains are written in upper case black and constituent cratonic blocks in lower case black. The study region in northern Quebec (blue box) is shown in more detail in Fig. 2a.

and a Palaeoproterozoic magmatic arc terrane, with plutonic (Narsajuaq arc) and volcanic (Parent Group) components[9] (Fig. 2a).

Granulite-facies metamorphism of the Superior basement was coeval with Neoarchaean plutonism at about 2.7 Ga (ref. 21). Rifting of the northern Superior craton occurred from 2.04–1.87 Ga, prior to collision with the Churchill plate at about 1.83 Ga, which resulted in thrust imbrication of the Superior craton margin strata to form the amphibolite-facies Cape Smith thrust belt (Fig. 2a)[21,22]. The Palaeoproterozoic amphibolite-facies metamorphism locally overprinted the Archaean granulite-facies metamorphism in the basement orthogneiss along zones of downward fluid migration[23]. Regional muscovite Ar–Ar ages of about 1.69–1.66 Ga indicate that this segment of the THO underwent slow cooling and exhumation[24]. Post-orogenic folding and refolding led to the formation of the basement-cored Kovik tectonic window of northern Quebec (Fig. 2a).

The studied retrogressed eclogite in the THO was sampled from the core of a metre-scale amphibolitized mafic boudin associated with metavolcaniclastic schist and Archaean basement orthogneiss in the Kovik window (starred locality, Fig. 2a). The amphibolitized boudins occur in curvilinear arrays, tens to hundreds of metres in length and striking approximately NW, which are hosted by well-layered felsic orthogneiss (Fig. 2b). The boudins are inferred to represent the northern extension of the undeformed, NW-striking Minto dyke swarm that was emplaced at $1,998 \pm 2$ Ma (ref. 25) during rifting of the Superior basement, and is well preserved south of the Kovik window (Fig. 2c). The metavolcaniclastic schist (Fig. 2d) forms part of the Povungnituk Group supracrustal strata, which are preserved within a moderately NNE dipping panel, tens of metres thick. The absence of a high-strain zone at the lower well-exposed orthogneiss/supracrustal contact, as well as

the complete lack of desegregation features, suggest structural coherency at the outcrop scale, indicating that the eclogite and schist retained their mutual primary tectonostratigraphic relationship during the entire subsequent metamorphic cycle. Both retrogressed eclogite (sample M85B) and schist (sample M85A) were therefore collected from the same outcrop to provide complementary insight into the P–T–time evolution of the region.

Eclogite and metavolcaniclastic schist petrography

Sample M85B is a retrogressed mafic eclogite, which contains garnet porphyroblasts in a matrix composed of relict omphacite, diopside–pargasite–plagioclase symplectites after omphacite, spinel–plagioclase±corundum symplectites after kyanite, and biotite (Supplementary Fig. 2). Garnet porphyroblasts form subhedral grains up to 1 cm in diameter, which are rimmed by pargasite–plagioclase intergrowths. Major element chemical traverses across the garnet porphyroblasts reveal that the interiors of cm-scale porphyroblasts are concentrically compositionally zoned, whereas mm-scale porphyroblasts are largely homogeneous, and that all garnet rims exhibit a local increase in the spessartine and Fe/(Fe+Mg) contents (Supplementary Fig. 3). These features suggest a single episode of prograde garnet growth before resorption[26], and varying degrees of size-dependent diffusional homogenization[27]. Biotite, chlorite, kyanite, quartz, rutile, zircon and zoisite are present as primary inclusions in garnet cores, and garnet rims contain biotite, kyanite, rutile, zircon and zoisite. Omphacite is present as minor, relict anhedral porphyroblasts in the matrix, with jadeite contents up to 0.31, which are embayed by retrograde diopside–pargasite–plagioclase symplectites (Supplementary Fig. 4)[28]. Plagioclase–spinel±corundum symplectites form tabular arrays surrounded by plagioclase haloes, typical of pseudomorphs after kyanite (Supplementary Figs 2 and 5)[29]. Ilmenite occurs as isolated grains and films around rutile in the matrix, and is interpreted as the retrograde replacement of peak rutile. Minor apatite and zircon are also present in the matrix, the latter typically marginal to retrograde ilmenite grains, indicating that zircon was reactive during metamorphism (Supplementary Fig. 6)[30,31].

Sample M85A is a metavolcaniclastic schist comprising garnet porphyroblasts in a matrix of biotite, cordierite, orthoamphibole (gedrite–anthophyllite), plagioclase and quartz (Supplementary Fig. 7a). Garnet porphyroblasts are present as anhedral grains up to 3 mm in diameter, which are surrounded by corona structures composed of radiating laths of orthoamphibole, cordierite and plagioclase (Supplementary Fig. 8). Chemical traverses across garnet porphyroblasts reveal flat, homogenized interior regions, and resorbed rim regions (Supplementary Fig. 9)[26]. The garnet grains contain pristine inclusions of apatite, biotite, quartz and rutile, as well as ragged sillimanite inclusions that are surrounded by cordierite and radiating cracks in the garnet host (Supplementary Fig. 7b,c). The sillimanite inclusions are interpreted as the polymorphic replacement of kyanite by sillimanite, which is a transition typified by cracking of rigid hosts due to the ∼10 vol.% increase[32], with the sillimanite subsequently replaced by cordierite. The absence of aluminosilicate in the matrix suggests that the garnet-hosted sillimanite is metastable and not part of the current equilibrium assemblage. Ilmenite is present throughout the matrix, with some grains containing rutile in their core regions, suggesting that rutile has been replaced by ilmenite in the matrix. Minor apatite, monazite and zircon are also present throughout the sample.

Phase diagram modelling and monazite geochronology

P–T equilibrium phase diagrams were constructed (Methods) for the metavolcaniclastic schist (M85A) and eclogite (M85B), with the intent of modelling both samples to constrain different segments of a composite P–T path. For sample M85A, H_2O was treated as in excess, due to the widespread presence of hydrous phases.
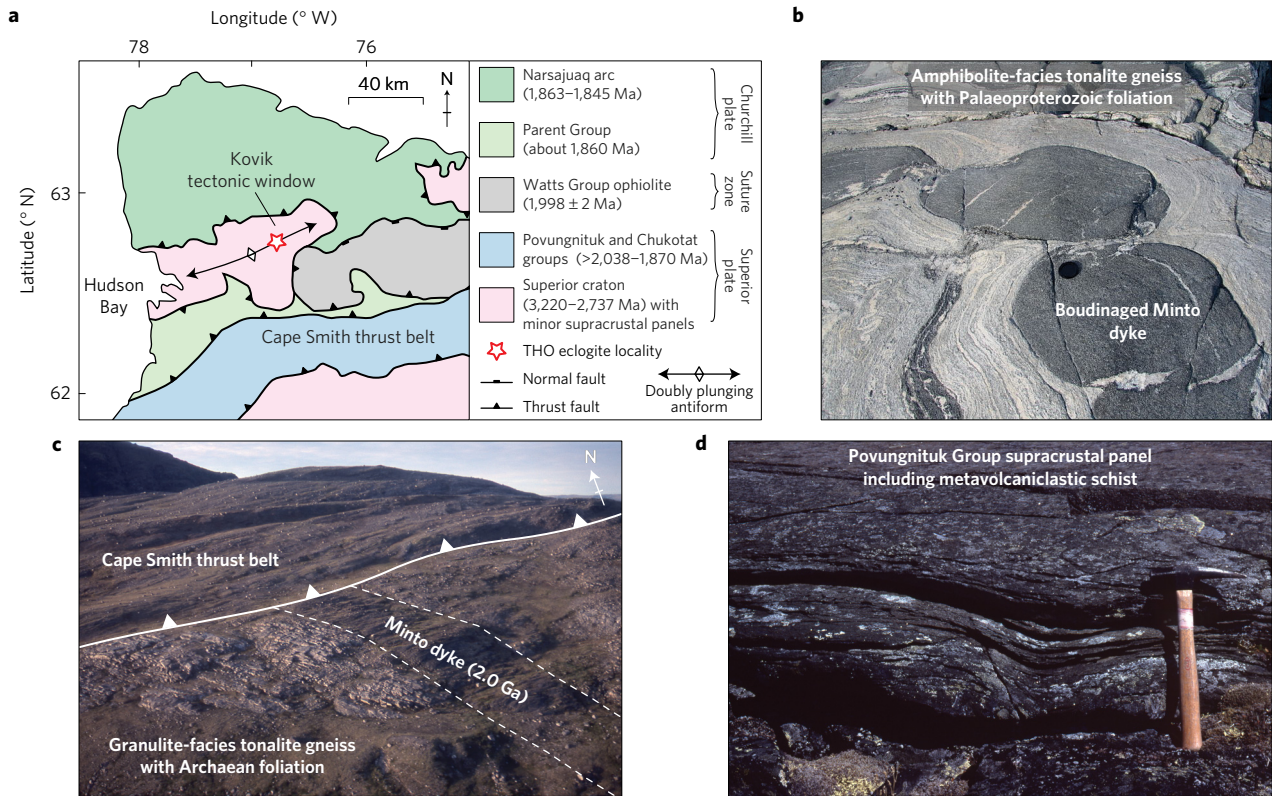
Figure 2 | Trans-Hudson eclogite geologic context. a, Simplified geologic map of northern Quebec[23]. The eclogite was sampled from an amphibolitized mafic boudin located within the Kovik tectonic window (starred locality). **b**, Photograph within the Kovik window, showing a boudinaged mafic dyke hosted by basement that exhibits Palaeoproterozoic amphibolite-facies overprint fabrics. **c**, Photograph at the toe of the Cape Smith thrust belt, showing an undeformed mafic dyke (~5 m thick) emplaced in basement that retains Archaean granulite-facies fabrics. **d**, Photograph within the Kovik window, showing the supracrustal panel from which the metavolcaniclastic schist was sampled (also starred locality).
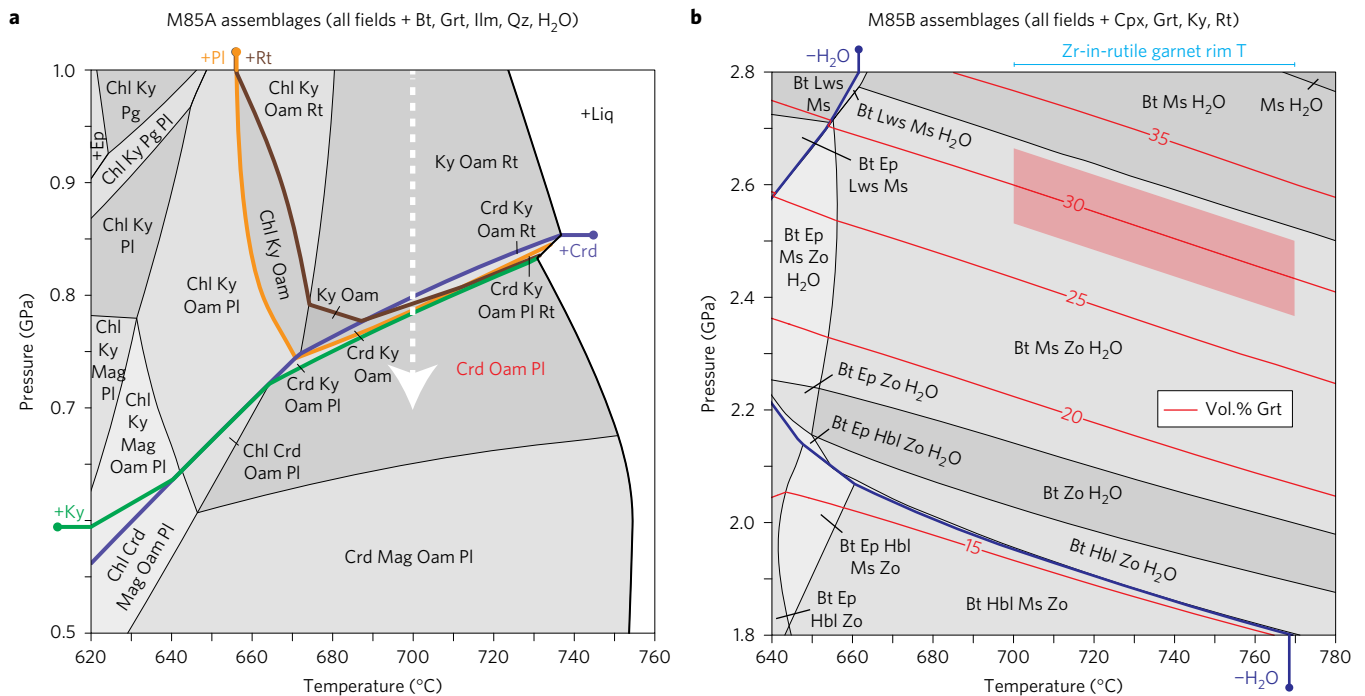

Figure 3 | P–T phase diagrams. a, M85A, calculated in the MnNCKFMASHTO model system. The observed assemblage is shown in red text. Petrographic observations of the former presence of rutile (brown line) and kyanite (green line), and the late growth of plagioclase (orange line) and cordierite (purple line) indicate an approach to the observed assemblage field from higher-pressure conditions (dashed white arrow). **b**, M85B, calculated in the NCKFMASHTO model system. Garnet vol.% isopleths (red lines) and the results of Zr-in-rutile thermometry[36,37] (light blue line; Supplementary Table 4) are used to define the peak P–T conditions (red area).
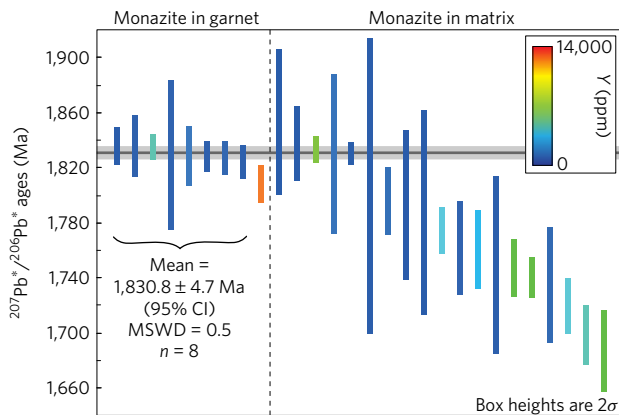
Figure 4 | M85A monazite geochronology results. Data are displayed by petrographic position of the analysed grains, sorted by decreasing age, and colour coded by Y content. Underlying data are given in Supplementary Table 7. *Radiogenic Pb. Concordia plot displayed in Supplementary Fig. 13e.

For sample M85B, the incomplete retrograde replacement of peak minerals suggests that H_2O availability during exhumation was limited[33]. Therefore, a value of $H_2O = 2.5$ mol.% was assigned, which represents the observed H_2O content of the sample (Methods). For both samples, the preserved mineral assemblages and their individual proportions, rather than mineral compositions, were the focus for determining metamorphic conditions, as the latter are demonstrably affected by retrograde diffusion-related processes[34,35]. In addition, Zr-in-rutile thermometry[36,37] was applied to sample M85B to help delimit peak metamorphic conditions.

A $P-T$ equilibrium phase diagram calculated for sample M85A reveals that the observed assemblage (red text, Fig. 3a) is stable from ~0.6 to 0.8 GPa, and 650 to 750 °C. At higher pressures, cordierite and plagioclase are predicted to leave the assemblage, and rutile and kyanite join the assemblage (coloured lines, Fig. 3a). Petrographic observations of the former presence of rutile and kyanite as inclusions in garnet (Supplementary Fig. 7b), and the late growth of plagioclase and cordierite in garnet corona textures (Supplementary Fig. 8), indicate an approach to the observed assemblage field from higher-pressure conditions (dashed white arrow, Fig. 3a and Supplementary Fig. 10).

For sample M85B, a peak assemblage cannot be definitively targeted in phase equilibria space (Fig. 3b), as the sample has been extensively overprinted. Nevertheless, petrographic analysis of the sample M85B matrix symplectites and garnet rim inclusion suite indicates that the peak assemblage contained at least biotite, garnet, kyanite, omphacite, rutile and zoisite. Zr-in-rutile thermometry applied to rutile located in garnet rims provides an effective means to assess the peak temperature conditions. Two thermometers are considered: one that takes into consideration the reduced activity of silica imposed by the absence of quartz from garnet rims[36], and another that can account for the pressure dependence of Zr-in-rutile[37]. The former thermometer yielded mean temperatures of 636 ± 9 to 685 ± 9 °C (95% CI, $n = 11$) over the plausible a_{SiO_2} range of 0.5 to 0.9 (Supplementary Table 4). The latter thermometer indicates that a pressure effect of $+74$ °C needs to be considered (at the suggested peak pressure below). Therefore, peak temperatures of ~700–770 °C are proposed (light blue bar, Fig. 3b).

To constrain pressure, the peak modal abundances of garnet (30 ± 2 vol.%), omphacite (47 ± 2 vol.%) and kyanite (13 ± 2 vol.%) were calculated (Supplementary Fig. 11). Although highly retrogressed, domains that were previously garnet, omphacite and kyanite are clear in their symplectite replacements. Notably, garnet mode exhibits the greatest pressure dependence (contours, Fig. 3b and Supplementary Fig. 12), and is the simplest to calculate
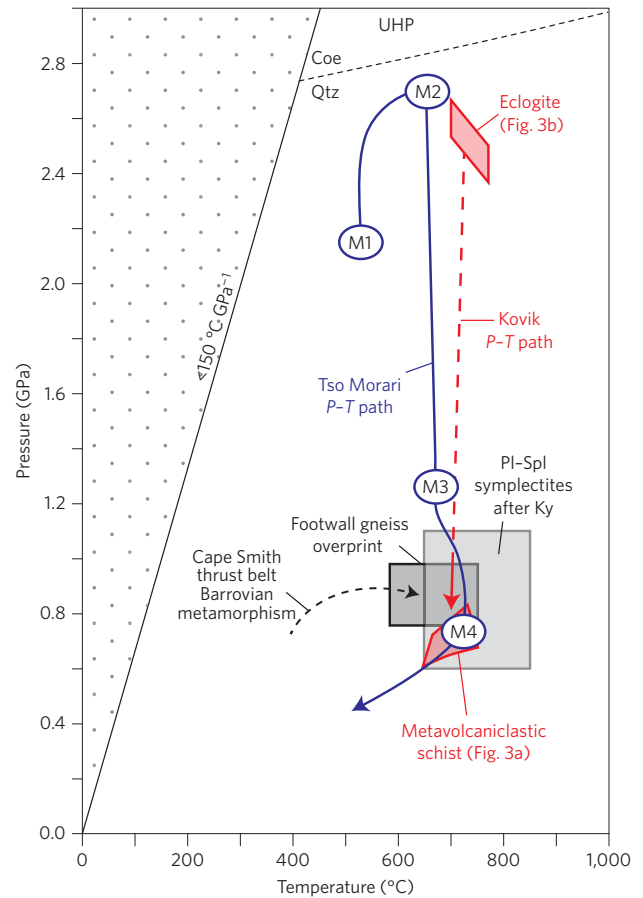

Figure 5 | $P-T$ results for the Palaeoproterozoic Trans-Hudson eclogite (red data) and relative correspondence with the Cenozoic Tso Morari eclogite (blue data). The inferred peak $P-T$ conditions of the Trans-Hudson eclogite (Fig. 3b) and retrograde equilibration of the metavolcaniclastic schist (Fig. 3a) are similar to the equivalent peak M2 and retrograde M4 conditions for non-coesite-bearing portions of the Himalayan Tso Morari eclogite massif[18]. Furthermore, the retrograde schist $P-T$ estimate is consistent with the formation of the spinel–plagioclase symplectites after kyanite in the eclogite (light grey area[29]), and the conditions of metamorphism associated with the base of the Cape Smith thrust belt (dark grey area[23]).

across a range of scales (thin section to hand sample), with the 30 ± 2 vol.% indicating peak pressures of ~2.35–2.65 GPa over the suggested peak temperature range (red area, Fig. 3b). This region is consistent with the inferred peak modal abundances of kyanite and omphacite, and satisfies the minimum peak assemblage constraint, with the addition of ~4 vol.% muscovite (Supplementary Fig. 12d). Although there is no petrographic record of muscovite in the sample, it is reasonable to consider that such a minor hydrous phase was consumed during retrograde overprinting[38], and the total mica content of the sample at peak conditions is consistent with the present biotite content of the sample (9 ± 2 vol.%). Consequently, conditions of ~2.50 ± 0.15 GPa and 735 ± 35 °C are suggested to be representative of peak metamorphism.

This $P-T$ range occupies H_2O-saturated conditions. Conversely, during exhumation the sample rapidly crosses into H_2O-undersaturated conditions (dark blue line, Fig. 3b), after which reaction kinetics would be sluggish[39], consistent with the development of symplectite structures in the sample. Studies of spinel–plagioclase–corundum symplectites after kyanite have shown that they form at 0.6–1.1 GPa and 650–850 °C (ref. 29), which provides a broad retrograde $P-T$ estimate for sample M85B.
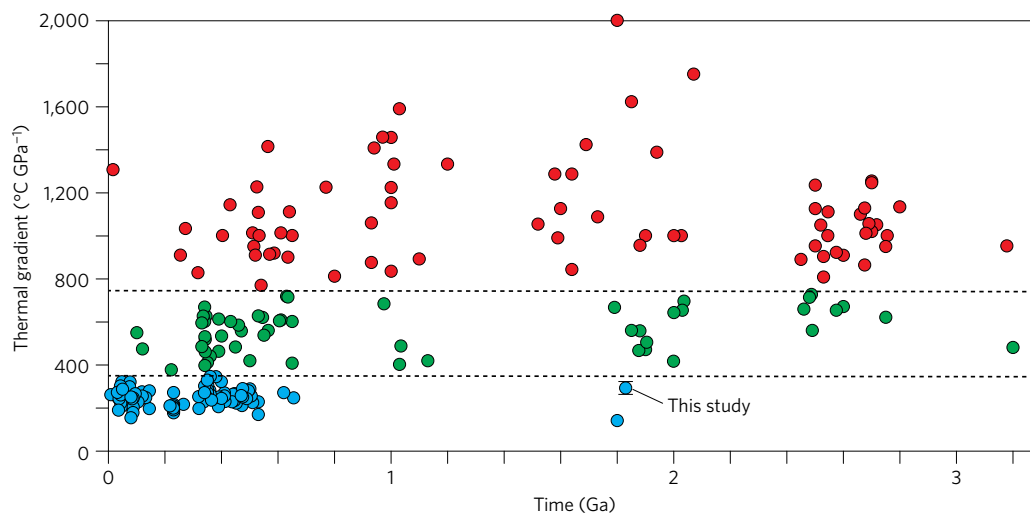
Figure 6 | Results of this study with respect to a global compilation[20] of metamorphic P–T–t data. A total of 215 P–T–t data points are grouped into three types of metamorphism: HP–UHP (blue data, <350 °C GPa^{-1}); eclogite–high-pressure granulite (green data); and granulite–ultrahigh temperature (red data, >750 °C GPa^{-1}). The data set[20] is supplemented by one more recent study of 1.8 Ga UHP metamorphism[44]. Uncertainty limits of this study datum correspond to the red shaded area of Fig. 3b. Note that older eclogites do exist[47–50], but these are all lower-pressure occurrences characterized by peak thermal gradients >350 °C GPa^{-1}, and are not demonstrably associated with continental subduction.

The suggested P–T conditions of final equilibration of sample M85A (0.7 ± 0.1 GPa and 700 ± 50 °C) fall within and refine this P–T range, and are also consistent with the peak metamorphic conditions associated with the base of the overlying Cape Smith thrust belt of 0.77–0.98 GPa and 585–755 °C (ref. 21).

To date the timing of metamorphism, *in situ* U–Pb isotopic analyses of monazite in sample M85A were carried out using a sensitive high-resolution ion microprobe (Methods). Monazite in sample M85A is present as inclusions in garnet grains, as well as throughout the matrix (Supplementary Fig. 13), and displays a range of textures, from homogeneous to sector-zoned (Supplementary Fig. 14). Twenty-eight analyses were made of 22 monazite grains in all petrographic positions in the sample (Supplementary Table 7). Monazite located in garnet grains yielded a tight cluster of ages, with relatively low Y contents, with a weighted mean ^{204}Pb-corrected ^{207}Pb/^{206}Pb age of 1,830.8 ± 4.7 Ma (MSWD=0.5, $n = 8$; excluding one high-Y chemical outlier, Fig. 4). Conversely, monazite analysed in the matrix yield a spread of ages, ranging from overlapping with the garnet-hosted monazite ages to as young as about 1,690 Ma, with the younger tail of ages associated with progressively higher Y contents.

Based on the presence of monazite as inclusions in garnet, and the relatively low Y contents of the analysed grains, the approximately 1,831 Ma monazite age is interpreted as a syn-garnet growth prograde age constraint for sample M85A, which provides a maximum age constraint for the timing of high-pressure eclogite-facies metamorphism in the region. Minimum age constraints for the eclogite-facies metamorphism are provided by: titanite, which is directly tied to amphibolite-facies corona textures in the basement gneisses, and is documented to have grown from about 1,814 to 1,789 Ma (ref. 40); and the age of Barrovian metamorphism bracketed between $1,820 + 4/ - 3$ and $1,815 ± 4$ Ma in the overlying Cape Smith thrust belt supracrustal units[11]. Consequently, eclogite-facies metamorphism in the region is constrained between about 1,831–1,820 Ma. The younger spread of ages present in the matrix is attributed to monazite that grew during retrograde metamorphism, with the increasing Y content due to the progressive resorption of garnet during decompression (Supplementary Figs 8 and 10). The tail of retrograde ages is also consistent with regional muscovite Ar–Ar ages of about 1.69–1.66 Ma, which indicate that this segment of the THO underwent slow cooling and exhumation[24].

Comparative tectonics and the metamorphic rock record

It is well established that the THO is broadly analogous to the Himalaya, with similarities in terms of scale (Fig. 1), seismic structure[12–14] and tectonostructural evolution[11,15]. This study adds detail to the comparison through the documentation of high-pressure, low-temperature metamorphism in the THO, which was previously lacking. The congruence is particularly striking between the THO eclogite locality and the Tso Morari eclogite locality in the western Himalaya, with both regions: comprising lower plate basement inliers exposed in suture zones (Supplementary Fig. 15a,c); preserving eclogite in the cores of metre-scale mafic boudins hosted by basement orthogneiss (Supplementary Fig. 15b,d)[18]; having experienced eclogite-facies metamorphism concomitant with the onset of collision (Supplementary Fig. 1)[10,11]; and featuring, in part, similar P–T cycles (Fig. 5).

Notably, peak P–T conditions at Tso Morari vary widely, from high-pressure conditions[18] similar to those documented for the THO eclogite of 2.50 ± 0.15 GPa and 735 ± 35 °C (Fig. 3b), to UHP conditions[41]. More work is required to determine if UHP conditions exist elsewhere within the Kovik tectonic window, as the boundaries of the high-pressure domain have yet to be established, and cryptic evidence for UHP metamorphism exists elsewhere in the THO[42]. One important distinction may obfuscate this search; although the retrograde P–T conditions are similar in both regions (Fig. 5)[18,28], exhumation of parts of the eastern THO occurred over at least 150 Myr (ref. 24), versus <50 Myr for Tso Morari. Potentially for this reason, eclogitic assemblages in the THO are more retrogressed. Nevertheless, we interpret the remarkable correspondence between the Palaeoproterozoic THO eclogite and the Cenozoic Tso Morari eclogite as reflecting the same underlying plate tectonic process (deep continental subduction and exhumation).

On a more global scale, analysis of peak metamorphic thermal gradients over time has been used to suggest that the late Neoproterozoic–Phanerozoic plate tectonic regime was different from the rest of the Proterozoic, with the former characterized by the first widespread appearance of cool thermal gradients (<350 °C GPa^{-1}; Fig. 6)[3–5,20]. However, the results of this study, which indicate peak thermal gradients of ~295 ± 30 °C GPa^{-1} at about 1.83 Ga, suggest that this distinction may be a false dichotomy, which probably exists due to the vulnerability of ancient high-pressure assemblages to overprinting/reworking and the

ravages of erosion. While the mantle has experienced secular cooling throughout its history, numerical modelling shows that the thermal structure of subduction zones is primarily controlled by the convergence rate and age of subducting lithosphere, with ambient mantle temperature imparting only a second-order effect, such that it is sensible to consider that high-pressure–low-temperature metamorphic conditions were traversed during the Proterozoic[43]. Therefore, we predict that further 'old and cold' data points will be located, if appropriate field areas are targeted for investigation. Notably, subtle evidence for ~1.8 Ga UHP metamorphism is preserved in west Greenland[44], and it has been suggested that the Kola Peninsula of northern Russia may have featured cool thermal gradients by at least 1.9 Ga (ref. 45) (although all aspects of the $P–T$–time evolution are disputed[46]). Further work is required on older samples to understand the dynamics of the early Earth, but for now the THO eclogite represents an important piece in the puzzle of past tectonic regimes, and does not support maintaining a metamorphic distinction between the Phanerozoic and Proterozoic eons.

Methods

Methods, including statements of data availability and any associated accession codes and references, are available in the online version of this paper.

References

1. Bédard, J. H., Harris, L. B. & Thurston, P. C. The hunting of the snArc. *Precambrian Res.* **229**, 20–48 (2013).
2. Polat, A. *et al*. The origin and compositions of Mesoarchean oceanic crust: evidence from the 3075 Ma Ivisaartoq greenstone belt, SW Greenland. *Lithos* **100**, 293–321 (2008).
3. Brown, M. Duality of thermal regimes is the distinctive characteristic of plate tectonics since the Neoarchean. *Geology* **34**, 961–964 (2006).
4. Stern, R. J. Evidence from ophiolites, blueschists, and ultrahigh-pressure metamorphic terranes that the modern episode of subduction tectonics began in Neoproterozoic time. *Geology* **33**, 557–560 (2005).
5. Brown, M. Metamorphic conditions in orogenic belts: a record of secular change. *Int. Geol. Rev.* **49**, 193–234 (2007).
6. Hoffman, P. F. United plates of America, the birth of a craton: early Proterozoic assembly and growth of Laurentia. *Annu. Rev. Earth Planet. Sci.* **16**, 543–603 (1988).
7. Lewry, J. & Stauffer, M. *The Early Proterozoic Trans-Hudson Orogen of North America* (Geological Association of Canada, Special Paper 37, 1990).
8. Corrigan, D., Pehrsson, S., Wodicka, N. & de Kemp, E. The Palaeoproterozoic Trans-Hudson orogen: a prototype of modern accretionary processes. *Geol. Soc. Lond. Spec. Pub.* **327**, 457–479 (2009).
9. St-Onge, M. R., Van Gool, J. A. M., Garde, A. A. & Scott, D. J. Correlation of Archaean and Palaeoproterozoic units between northeastern Canada and western Greenland: constraining the pre-collisional upper plate accretionary history of the Trans-Hudson orogen. *Geol. Soc. Lond. Spec. Pub.* **318**, 193–235 (2009).
10. Green, O., Searle, M. P., Corfield, R. I. & Corfield, R. M. Cretaceous-Tertiary carbonate platform evolution and the age of the India-Asia collision along the Ladakh Himalaya (northwest India). *J. Geol.* **116**, 331–353 (2008).
11. St-Onge, M. R., Searle, M. P. & Wodicka, N. Trans-Hudson orogen of North America and Himalaya-Karakoram-Tibetan orogen of Asia: structural and thermal characteristics of the lower and upper plates. *Tectonics* **25**, 1–22 (2006).
12. Eaton, D. W. & Darbyshire, F. Lithospheric architecture and tectonic evolution of the Hudson Bay region. *Tectonophysics* **480**, 1–22 (2010).
13. Thompson, D. A. *et al*. Precambrian crustal evolution: seismic constraints from the Canadian Shield. *Earth Planet. Sci. Lett.* **297**, 655–666 (2010).
14. Bastow, I. D. *et al*. Precambrian plate tectonics: seismic evidence from northern Hudson Bay, Canada. *Geology* **39**, 91–94 (2011).
15. Corrigan, D. in *Tectonic Styles in Canada: The LITHOPROBE Perspective* (eds Percival, J. A., Cook, F. & Clowes, R.) Ch. 4, 237–284 (Geological Association of Canada, Special Paper 49, 2012).
16. Parrish, R. R., Gough, S., Searle, M. P. & Waters, D. J. Plate velocity exhumation of ultrahigh-pressure eclogites in the Pakistan Himalaya. *Geology* **34**, 989–992 (2006).
17. Lanari, P. *et al*. Deciphering high-pressure metamorphism in collisional context using microprobe mapping methods: application to the Stak eclogitic massif (northwest Himalaya). *Geology* **41**, 111–114 (2013).
18. St-Onge, M. R., Rayner, N., Palin, R. M., Searle, M. P. & Waters, D. J. Integrated pressure–temperature–time constraints for the Tso Morari dome (northwest India): implications for the burial and exhumation path of UHP units in the western Himalaya. *J. Metamorph. Geol.* **31**, 469–504 (2013).
19. Brown, M. in *When did Plate Tectonics Begin on Planet Earth?* (eds Condie, K. C. & Pease, V.) 97–128 (Geological Society of America, Special Paper 440, 2008).
20. Brown, M. The contribution of metamorphic petrology to understanding lithosphere evolution and geodynamics. *Geosci. Front.* **5**, 553–569 (2014).
21. St-Onge, M. R. & Ijewliw, O. J. Mineral corona formation during high-*P* retrogression of granulitic rocks, Ungava orogen, Canada. *J. Petrol.* **37**, 553–582 (1996).
22. Lucas, S. B. Structural evolution of the Cape Smith thrust belt and the role of out-of-sequence faulting in the thickening of mountain belts. *Tectonics* **8**, 655–676 (1989).
23. St-Onge, M. R. & Lucas, S. B. Large-scale fluid infiltration, metasomatism and re-equilibration of Archaean basement granulites during Palaeoproterozoic thrust belt construction, Ungava orogen, Canada. *J. Metamorph. Geol.* **13**, 509–535 (1995).
24. Skipton, D., Schneider, D., Kellett, D. & Joyce, N. *New Insights on the Cooling History of Hall Peninsula, Southern Baffin Island, Nunavut, using Ar Thermochronology on Muscovite* 17–30 (Canada-Nunavut Geoscience Office, 2015).
25. Buchan, K. L., Mortensen, J. K., Card, K. D. & Percival, J. A. Paleomagnetism and U–Pb geochronology of diabase dyke swarms of Minto block, Superior Province, Quebec, Canada. *Can. J. Earth Sci.* **35**, 1054–1069 (1998).
26. Kohn, M. J. & Spear, F. S. Retrograde net transfer reaction insurance for pressure–temperature estimates. *Geology* **28**, 1127–1130 (2000).
27. Caddick, M. J., Konopasek, J. & Thompson, A. B. Preservation of garnet growth zoning and the duration of prograde metamorphism. *J. Petrol.* **51**, 2327–2347 (2010).
28. Palin, R., St-Onge, M., Waters, D., Searle, M. & Dyck, B. Phase equilibria modelling of retrograde amphibole and clinozoisite in mafic eclogite from the Tso Morari massif, northwest India: constraining the $P–T–M(H_2O)$ conditions of exhumation. *J. Metamorph. Geol.* **32**, 675–693 (2014).
29. Baldwin, J. A., Powell, R., White, R. W. & Štípská, P. Using calculated chemical potential relationships to account for replacement of kyanite by symplectite in high pressure granulites. *J. Metamorph. Geol.* **33**, 311–330 (2015).
30. Bingen, B., Austrheim, H. & Whitehouse, M. Ilmenite as a source for zirconium during high-grade metamorphism? Textural evidence from the Caledonides of western Norway and implications for zircon geochronology. *J. Petrol.* **42**, 355–375 (2001).
31. Weller, O. M. *et al*. U–Pb zircon geochronology and phase equilibria modelling of a mafic eclogite from the Sumdo complex of south-east Tibet: insights into prograde zircon growth and the assembly of the Tibetan plateau. *Lithos* **262**, 729–741 (2016).
32. Skinner, B. J., Clark, S. P. & Appleman, D. E. Molar volumes and thermal expansions of andalusite, kyanite, and sillimanite. *Am. J. Sci.* **259**, 651–668 (1961).
33. Zhang, R. Y., Liou, J. G., Zheng, Y. F. & Fu, B. Transition of UHP eclogites to gneissic rocks of low-amphibolite facies during exhumation: evidence from the Dabie terrane, central China. *Lithos* **70**, 269–291 (2003).
34. Powell, R., Guiraud, M. & White, R. W. Truth and beauty in metamorphic phase-equilibria: conjugate variables and phase diagrams. *Can. Mineral.* **43**, 21–33 (2005).
35. Palin, R. M., Weller, O. M., Waters, D. J. & Dyck, B. Quantifying geological uncertainty in metamorphic phase equilibria modelling; a Monte Carlo assessment and implications for tectonic interpretations. *Geosci. Front.* **7**, 591–607 (2016).
36. Ferry, J. M. & Watson, E. B. New thermodynamic models and revised calibrations for the Ti-in-zircon and Zr-in-rutile thermometers. *Contrib. Mineral. Petrol.* **154**, 429–437 (2007).
37. Tomkins, H. S., Powell, R. & Ellis, D. J. The pressure dependence of the zirconium-in-rutile thermometer. *J. Metamorph. Geol.* **25**, 703–713 (2007).
38. Clarke, G. L., Powell, R. & Fitzherbert, J. A. The lawsonite paradox: a comparison of field evidence and mineral equilibria modelling. *J. Metamorph. Geol.* **24**, 715–725 (2007).
39. Guiraud, M., Powell, R. & Rebay, G. H_2O in metamorphism and unexpected behaviour in the preservation of metamorphic mineral assemblages. *J. Metamorph. Geol.* **19**, 445–454 (2001).
40. Scott, D. J. & St-Onge, M. R. Constraints on Pb closure temperature in titanite based on rocks from the Ungava orogen, Canada: implications for U–Pb geochronology and P-T-t path determinations. *Geology* **23**, 1123–1126 (1995).

41. Wilke, F. D., O'Brien, P. J., Schmidt, A. & Ziemann, M. A. Subduction, peak and multi-stage exhumation metamorphism: traces from one coesite-bearing eclogite, Tso Morari, western Himalaya. *Lithos* **231,** 77–91 (2015).
42. Cartigny, P., Chinn, I., Viljoen, K. S. & Robinson, D. Early Proterozoic ultrahigh pressure metamorphism: evidence from microdiamonds. *Science* **304,** 853–855 (2004).
43. Peacock, S. M. in *Inside the Subduction Factory* Vol. 138 (ed. Eiler, J.) 7–22 (American Geophysical Union, 2004).
44. Glassley, W. E., Korstgard, J. A., Storensen, K. & Platou, S. W. A new UHP metamorphic complex in the ∼1.8 Ga Nagssugtoqidian orogen of west Greenland. *Am. Mineral.* **99,** 1315–1334 (2014).
45. Morgunova, A. & Perchuk, A. Ultrahigh-pressure metamorphism in the Archean–Proterozoic Mobile Belt (Gridino Complex, Karelia, Russia). *Dokl. Earth Sci.* **443,** 412–416 (2012).
46. Kaulina, T. V., Yapaskurt, V. O., Presnyakov, S. L., Savchenko, E. E. & Simakin, S. G. Metamorphic evolution of the Archean eclogite-like rocks of the Shirokaya and Uzkaya Salma area (Kola Peninsula): geochemical features of zircon, composition of inclusions, and age. *Geochem. Int.* **48,** 871–890 (2010).
47. Moller, A., Appel, P., Mezger, K. & Schenk, V. Evidence for a 2 Ga subduction zone: eclogites in the Usagaran belt of Tanzania. *Geology* **23,** 1067–1070 (1995).
48. Baldwin, J. A., Powell, R., Williams, M. L. & Goncalves, P. Formation of eclogite, and reaction during exhumation to mid-crustal levels, Snowbird tectonic zone, western Canadian shield. *J. Metamorph. Geol.* **25,** 953–974 (2007).
49. Mints, M. V. *et al*. Mesoarchean subduction processes: 2.87 Ga eclogites from the Kola Peninsula, Russia. *Geology* **38,** 739–742 (2010).
50. Ganne, J. *et al*. Modern-style plate subduction preserved in the Palaeoproterozoic West African craton. *Nat. Geosci.* **5,** 60–65 (2012).

Author contributions
O.M.W. collected data, performed the calculations and wrote the paper; M.R.S.-O. conceived the idea, collected data and conducted the fieldwork. Both authors analysed the data.

Additional information
Supplementary information is available in the online version of the paper. Reprints and permissions information is available online at www.nature.com/reprints. Correspondence and requests for materials should be addressed to O.M.W.

Competing financial interests
The authors declare no competing financial interests.

Methods

Petrography and mineral chemistry. The studied eclogite (GSC sample number SAB91-M85B, hereafter M85B) and metavolcaniclastic schist (GSC sample number SAB91-M85A, hereafter M85A) were collected from the same locality (Fig. 2a; 76°42′ 13.8″ W, 61°44′ 5.1″ N).

Petrography. Representative images of microstructural features and assemblages are given in Supplementary Figs 2–9. Phase maps (Supplementary Figs 5a and 8) were produced using a Zeiss Evo scanning electron microscope (SEM) at the Geological Survey of Canada (GSC) equipped with Oxford Instruments' Aztec software (v2.2) AutoPhaseMap routine. Modal abundances of major rock-forming minerals were calculated using the phase maps, and by point counting thin sections and polished hand-specimen surface images with randomized 500-point grids using the software JMicroVision[51]. Raman spectra of aluminosilicate polymorphs were obtained at the Surface Nanoengineering Lab, Ottawa University, with an integrated micro/macro-WITec 300 RSA confocal Raman equipped with a 532 nm solid-state Nd:YAG laser (grating 600 grooves mm^{-1}). The laser spot size was focused to the surface with a 20× objective. Spatial resolution is ∼5 μm and the output power of 35 mW produces an irradiation power of ∼10–15 mW on the sample. Raman spectra were collected in ten accumulations of 10 s each. Calibration was performed using the 532 nm Rayleigh line.

Whole-rock chemistry. Whole-rock major element oxides (Supplementary Table 1) were determined by lithium metaborate/tetraborate fusion inductively coupled plasma (ICP) whole-rock analysis using a Perkin Elmer Sciex ELAN 6000 ICP/MS at Activation Laboratories, Ancaster. 1 kg of each study sample was crushed in an agate mill for analysis. FeO (hence $X_{Fe^{3+}} = Fe^{3+}/(Fe^{2+} + Fe^{3+})$; Supplementary Table 1) was calculated by wet titration using a cold acid digestion of ammonium metavanadate and hydrofluoric acid in an open system. Ferrous ammonium sulfate was added after digestion and potassium dichromate was the titrating agent.

Mineral chemistry. Major element mineral compositional analyses (Supplementary Tables 2 and 3) were acquired on a JEOL JXA-8230 electron probe microanalyser (EPMA) equipped with five wavelength-dispersive spectrometers at the Department of Earth and Environmental Sciences, Ottawa University, using operating conditions of 20 kV accelerating voltage and 20 nA current. Standards were a mix of natural and synthetic minerals and metals, and a correction procedure was applied[52]. All mineral cation totals were calculated using AX[53]. Anhydrous mineral compositions were calculated to standard numbers of oxygen per formula unit (pfu), whereas mica analyses were calculated to a total of 11, chlorite to 14, cordierite to 18, amphibole to 23 and zoisite to 25. Mineral abbreviations follow convention[54].

Trace element analyses of rutile (Supplementary Table 4) were acquired using a Laser Ablation Inductively Coupled Plasma Mass Spectrometer (LA–ICP–MS) at the Geological Survey of Canada. The system consists of a Teledyne Photon Machines Analyte G2 excimer LA system ($\lambda = 193$ nm) with HelEx ablation cell and an Agilent 7700x ICP–MS equipped with a second rotary vacuum pump that improves instrument sensitivity across the mass range by a factor of 2–3 times[55]. The USGS doped basaltic glass GSE-1G[56] was used as calibration standard; BCR-2G as quality control standard. Detailed operating parameters in LA–ICP–MS analysis of rutile are given in Supplementary Table 5. The data reduction was performed using GLITTER[57]. The 'GeoReM preferred values' (February 2010) from the on-line geologic and environmental reference materials database, GeoReM[58], were used for the concentrations of the elements in GSD-1G and BCR-2G. The Ti content was used as an internal standard.

Phase diagram modelling. Phase diagrams were constructed using THERMOCALC v3.40 with the internally consistent thermodynamic data set ds55 (updated to August 2004)[59,60]. The bulk-rock compositions used for modelling (Supplementary Table 6) were calculated by modification of whole-rock ICP–MS analyses (Supplementary Table 1). For both samples, the preserved mineral assemblages and their individual proportions, rather than mineral compositions, were the focus for determining metamorphic conditions, as the latter are demonstrably affected by retrograde diffusion-related processes[34,35]. Fractionated garnet growth was not incorporated into the modelling due to uncertainties over the prograde $P–T$ conditions of nucleation as a result of the significant retrograde diffusional modification of the garnet chemistry (Supplementary Figs 3 and 9).

For M85A, modelling was performed in the 11-component MnO–Na$_2$O–CaO–K$_2$O–FeO–MgO–Al$_2$O$_3$–SiO$_2$–H$_2$O–TiO$_2$–O$_2$ (MnNCKFMASHTO) system using the following activity–composition (a–x) relations for solid-solution phases: biotite, garnet and haematite–ilmenite[61]; chlorite[62]; cordierite and epidote[60]; gedrite–anthophyllite[63]; magnetite[64]; plagioclase–K-feldspar[65]; and muscovite–paragonite[66]. Pure phases included kyanite, H$_2$O, quartz, rutile and sillimanite. The CaO total from the whole-rock ICP–MS analysis was modified[67] by assuming that half of the measured P$_2$O$_5$ was derived from apatite (with the rest from monazite). Only sub-solidus phase relations were calculated for sample M85A, due to the absence of evidence for present or former melt-bearing assemblages. H$_2$O was treated as in excess, due to the widespread presence of prograde, peak and retrograde hydrous phases. The

orthoamphibole (Oam) endmembers are not differentiated on Fig. 3a as the considered temperature range is above the gedrite–anthophyllite solvus, and the compositions of the calculated Oam are intermediate.

For M85B, modelling was performed in the 10-component Na$_2$O–CaO–K$_2$O–FeO–MgO–Al$_2$O$_3$–SiO$_2$–H$_2$O–TiO$_2$–O$_2$ (NCKFMASHTO) system using the following a–x relations for solid-solution phases: actinolite–cummingtonite–glaucophane–hornblende and diopside–omphacite–jadeite[63]; biotite and garnet[68]; chlorite[62]; epidote[60]; and muscovite–paragonite[66]. Pure phases included coesite, H$_2$O, lawsonite, quartz and rutile. MnO was not included as a component as the lack of Mn-bearing activity models for other major eclogite-facies minerals (amphibole, clinopyroxene and white mica) precludes examination of partitioning between these phases[18]. The CaO total from the whole-rock ICP–MS analysis was modified by assuming that all P$_2$O$_5$ was derived from apatite. The incomplete retrograde replacement of peak minerals such as omphacite (Supplementary Fig. 4) suggests that H$_2$O availability during exhumation was limited (see refs 28,33). Therefore, a value of H$_2$O = 2.5 mol.% was assigned, which represents an estimate of the present H$_2$O content of the sample. This was calculated by combining compositional analyses of major phases (with H$_2$O assumed to be present in stoichiometric proportions in hydrous phases; Supplementary Table 2) in proportion to their volume in the rock. The proportion of each considered phase was calculated by a combination of point counting and phase area mapping. The clinopyroxene (Cpx) endmembers are not differentiated on Fig. 3b as the considered temperature range is above the diopside–omphacite solvus, and the compositions of the calculated Cpx are intermediate (Supplementary Fig. 12a).

Geochronology. *In situ* U–Pb isotopic analyses of monazite in sample M85A were carried out using a sensitive high-resolution ion microprobe (SHRIMP), which preserves the petrographic context of obtained age data, at the GSC. Automated full thin-section scans were performed on the GSC's Zeiss Evo SEM to locate monazite suitable for geochronological analysis. Targets from all petrographic contexts were prepared for analysis by coring multiple thin sections using a diamond-tipped drill bit and mounting in epoxy[69]. Backscattered electron images and X-ray Y, Th, Ce and U maps were generated for each monazite grain (using the EMPA set-up described above), to identify internal compositional domains, and to guide analytical spot placement[70]. Analytical details regarding spot size, data reduction protocol and U–Pb calibration are reported as footnotes in Supplementary Table 7. Isoplot (version 3.0)[71] was used to generate mean ages with related statistics. ^{207}Pb*/^{206}Pb* dates are reported as these provide the most precise age estimate for Palaeoproterozoic rocks[72,73].

The feasibility of dating zircon in the eclogite was assessed. However, impediments to this approach were the scarcity, small size and low U contents of the zircon grains (most <50 ppm). By considering the primary beam intensity and U content of the grains, the anticipated precision based only on counting statistic errors was ∼±130 Ma (2σ). This is a best-case scenario for the precision, as it does not include error associated with the common Pb correction, which could also be significant in these low-U zircons. These large errors, in conjunction with minimal targets, meant that zircon dating could not usefully contribute to constraining the age of the eclogite, and thus was not attempted further.

Code availability. The software used to generate the phase diagrams can be downloaded at http://www.metamorph.geo.uni-mainz.de/thermocalc.

Data availability. The data files used to generate the phase diagrams can be downloaded at http://www.metamorph.geo.uni-mainz.de/thermocalc.

References

51. Roduit, N. *JMicroVision: Image Analysis Toolbox for Measuring and Quantifying Components of High-Definition Images* Version 1.2.8 (2010); http://www.jmicrovision.com

52. Pouchou, J.-L. & Pichoir, F. in *Electron Probe Quantification* (eds Heinrich, K. & Newbury, D.) 31–75 (Plenum, 1991).

53. Holland, T. J. B. *AX: A Program to Calculate Activities of Mineral End-Members from Chemical Analyses* (2009); http://www.esc.cam.ac.uk/research/research-groups/research-projects/tim-hollands-software-pages/ax

54. Whitney, D. L. & Evans, B. W. Abbreviations for names of rock-forming minerals. *Am. Mineral.* **95,** 185–187 (2010).

55. Cabri, L. & Jackson, S. New developments in characterization of sulphide refractory Au ores. In *MetSoc World Gold 2011 50th Conf. Metallurgists* 51–62 (MetSoc, 2011).

56. Guillong, M., Hametner, K., Reusser, E., Wilson, S. a. & Günther, D. Preliminary characterisation of new glass reference materials (GSA-1G, GSC-1G, GSD-1G and GSE-1G) by laser ablation-inductively coupled plasma-mass spectrometry using 193 nm, 213 nm and 266 nm wavelengths. *Geostand. Geoanal. Res.* **29,** 315–331 (2005).

57. Griffin, W. L., Powell, W. L., Pearson, N. J. & O'Reilly, S. Y. in *Laser Ablation-ICP Mass Spectrometry in the Earth Sciences: Current Practises and Outstanding Issues* (ed. Sylvester, P.) 308–311 (Mineralogical Association of Canada, 2008).

58. Jochum, K. P. *et al*. GeoReM: a new geochemical database for reference materials and isotopic standards. *Geostand. Geoanal. Res.* **29,** 333–338 (2005).

59. Powell, R. & Holland, T. J. B. An internally consistent dataset with uncertainties and correlations: 3. Applications to geobarometry, worked examples and a computer program. *J. Metamorph. Geol.* **6,** 173–204 (1988).

60. Holland, T. J. B. & Powell, R. An internally consistent thermodynamic data set for phases of petrological interest. *J. Metamorph. Geol.* **16,** 309–343 (1998).

61. White, R. W., Pomroy, N. E. & Powell, R. An *in situ* metatexite-diatexite transition in upper amphibolite facies rocks from Broken Hill, Australia. *J. Metamorph. Geol.* **23,** 579–602 (2005).

62. Holland, T., Baker, J. & Powell, R. Mixing properties and activity–composition relationships of chlorites in the system $MgO–FeO–Al_2O_3–SiO_2–H_2O$. *Eur. J. Mineral.* **10,** 395–406 (1998).

63. Diener, J. F. A. & Powell, R. Revised activity–composition models for clinopyroxene and amphibole. *J. Metamorph. Geol.* **30,** 131–142 (2012).

64. White, R. W., Powell, R., Holland, T. J. B. & Worley, B. A. The effect of TiO_2 and Fe_2O_3 on metapelitic assemblages at greenschist and amphibolite facies conditions: mineral equilibria calculations in the system $K_2O–FeO–MgO–Al_2O_3–SiO_2–H_2O–TiO_2–Fe_2O_3$. *J. Metamorph. Geol.* **18,** 497–511 (2000).

65. Holland, T. J. B. & Powell, R. Activity–composition relations for phases in petrological calculations: an asymmetric multicomponent formulation. *Contrib. Mineral. Petrol.* **145,** 492–501 (2003).

66. Coggon, R. & Holland, T. J. B. Mixing properties of phengitic micas and revised garnet–phengite thermobarometers. *J. Metamorph. Geol.* **20,** 683–696 (2002).

67. Weller, O. M. *et al*. Quantifying Barrovian metamorphism in the Danba structural culmination of eastern Tibet. *J. Metamorph. Geol.* **31,** 909–935 (2013).

68. White, R. W., Powell, R. & Holland, T. J. B. Progress relating to calculation of partial melting equilibria for metapelites. *J. Metamorph. Geol.* **25,** 511–527 (2007).

69. Rayner, N. M. & Stern, R. A. *Improved Sample Preparation Method for SHRIMP Analysis of Delicate Mineral Grains Exposed in Thin Sections* Radiogenic Age and Isotopic Studies Report 15, Current Research 2002-F10 (Geological Survey of Canada, 2002).

70. Stern, R. A. & Berman, R. G. Monazite U–Pb and Th–Pb geochronology by ion microprobe, with an application to *in situ* dating of an Archean metasedimentary rock. *Chem. Geol.* **172,** 113–130 (2000).

71. Ludwig, K. *User's Manual for Isoplot/Ex rev. 3.00: a Geochronological Toolkit for Microsoft Excel* (Berkeley Geochronology Center, 2003).

72. Mattinson, J. M. U–Pb ages of zircons: a basic examination of error propagation. *Chem. Geol.* **66,** 151–162 (1987).

73. Schoene, B. in *Treatise on Geochemistry* Vol. 4 2nd edn (eds Holland, H. & Turekian, K.) 341–378 (2014).